1997MNRAS.284..137L

Mon. Not. R. Astron. Soc. **284**, 137–147 (1997)

Shaping of nova remnants by binary motion

H. M. Lloyd, T. J. O'Brien and M. F. Bode

Astrophysics Group, Electrical Engineering, Electronics and Physics, Liverpool John Moores University, Byrom Street, Liverpool L3 3AF

Accepted 1996 August 8. Received 1996 July 11; in original form 1996 March 28

ABSTRACT

We present the results of 2.5D hydrodynamic calculations of the effects of the underlying binary system on shaping the ejecta in a classical nova outburst. In the model, the outburst takes place in the form of a wind with secularly increasing velocity. This wind flows past a binary companion, which experiences a frictional drag force and transfers energy and angular momentum from its orbit into the expanding envelope. We find that many of the features seen in classical nova remnants can be reproduced, including polar blobs, polar rings and shells with tropical and equatorial bands. The features seen in the shells correlate with speed class in the observed manner – fast novae produce spherical shells, whereas slower novae produce banded shells and polar blobs. The effects of radiative cooling and the Rayleigh–Taylor instability on the shells are discussed. It is found that, as observations appear to indicate, the shells of fast novae should comprise a few, large clumps, whereas the shells of slower novae will be clumped on scales which are small compared to the shell radius.

Key words: hydrodynamics – instabilities – binaries: general – stars: mass-loss – novae, cataclysmic variables.

1 INTRODUCTION

Classical novae occur in semidetached binary systems containing a main-sequence star, which fills its Roche Lobe, and a white dwarf. Matter transferred on to the white dwarf builds up until nuclear burning commences under degenerate conditions, leading to a thermonuclear runaway and the subsequent ejection of $\sim 10^{-4}\,\mathrm{M}_\odot$ of material at velocities of a few hundred to a few thousand km s^{-1} (see, e.g., Bode & Evans 1989). Several years after outburst, extended optical emission can be seen around many classical novae. This usually takes the form of a shell, with aspherical symmetry. Common features include equatorial rings, polar caps and, at least in the case of DQ Herculis, pronounced tropical rings above and below the equatorial band. The latest images of DQ Her (Slavin, O'Brien & Dunlop 1995) show all of these features along with an extended diffuse halo, and 'cometary tails' extended radially outward from clumps within the shell. The degree of asymmetry in the optical remnant of a nova is also strongly correlated with the speed class of the outburst (Slavin et al. 1995) – fast novae have remnants with aspect ratios closer to unity than those of slow novae.

An attractive possibility for explaining the departure from spherical symmetry is the effect of the binary companion. The photospheric radius of the nova ejecta is greater than the binary separation for several weeks or months after the outburst, and there is therefore a lengthy 'common-envelope' phase in which the ejected matter will interact with the secondary star (e.g. MacDonald 1980, 1986; Livio et al. 1990; Shankar, Livio & Truran 1991). The secondary star experiences a frictional drag force in the nova envelope, and transfers orbital energy and angular momentum to the ejecta, causing the material to be ejected in a highly anisotropic flow. Previous 2D calculations of the effects of the secondary star on nova mass-loss (Livio et al. 1990) assumed a hydrostatic envelope, and are therefore more likely to be appropriate to the case of a slow nova, in which the velocity of ejection is low. In this case it was found that the nova envelope was ejected in the plane of the binary orbit, with very little mass-loss in the polar direction. In this paper, we present 2.5D numerical hydrodynamic calculations which investigate the effects of the binary system on mass ejection in faster novae, where the ejecta will already have a significant expansion velocity before the effects of energy deposition by the secondary star are taken into account. We also discuss the effects of radiative cooling of shocked gas in the ejecta, and the subsequent shredding of the shell by the Rayleigh–Taylor instability.

2 THE MODEL

2.1 Mass ejection

Mass ejection in novae can be well modelled by an optically thick, transonic wind (e.g. Bath & Harkness 1989; Kato & Hachisu 1994, and references therein). Typically, these winds reach terminal velocity at a radius which is comparable to the binary separation for a nova system, and we therefore assume a steady wind as the initial condition for our calculations. The wind velocity does not remain constant, however. There is strong evidence to point to the fact that the ejection velocity in novae increases with time. Spectral lines observed during outburst show increasing velocities. Also, X-ray emission from hot, shocked gas observed 5 d after the outburst of Nova Herculis 1991 (Lloyd et al. 1992) could be explained only in terms of the interaction of ejecta components with differing velocities (O'Brien, Lloyd & Bode 1994). The diffuse halo and cometary tails recently observed in DQ Her also provide evidence for a secular increase in ejection velocity – the diffuse halo is possibly composed of material which has overtaken the main shell, forming cometary tails via ablation of the shell. A detailed spectroscopic investigation of nova V1974 Cygni (Chochol et al., preprint) shows that the Orion system of absorptions can be associated with material which is closer to the central star than the material responsible for the principal absorption system, which shows lower radial velocities. Furthermore, thermonuclear runaway calculations (Kovetz & Prialnik 1994; Prialnik & Kovetz 1995) show that the velocity of ejection should increase with time, accompanied by a decrease in mass-loss rate. Similar behaviour is encountered in the detailed optically thick wind models of Kato & Hachisu (1994).

In the model, we assume that the mass-loss rate and velocity in the wind take the form

$$\dot{M}=\begin{cases}\dot{M}_0 & t<t_0\\ \dot{M}_0+\dfrac{t-t_0}{t_1-t_0}\,(\dot{M}_1-\dot{M}_0) & t_0\leq t<t_1\\ \dot{M}_1 & t\geq t_1\end{cases} \qquad (1)$$

and

$$v=\begin{cases}v_0 & t<t_0\\ v_0+\dfrac{t-t_0}{t_1-t_0}\,(v_1-v_0) & t_0\leq t<t_1.\\ v_1 & t\geq t_1\end{cases} \qquad (2)$$

2.2 Energy deposition

The drag energy deposition rate is calculated using the prescription of Livio & Soker (1988). The drag luminosity is therefore given by

$$L_{\mathrm{d}}=\xi\pi R_{\mathrm{a}}^2\rho v_{\mathrm{r}}^3, \qquad (3)$$

where ρ is the gas density, v_{r} is the relative velocity of the secondary with respect to the wind, ξ is a drag coefficient of order unity, and R_{a} is the Bondi–Hoyle accretion radius given by

$$R_{\mathrm{a}}=\frac{2GM_2}{v_{\mathrm{r}}^2+c^2}, \qquad (4)$$

where M_2 is the mass of the secondary star, and c is the speed of sound in the gas. The exact value of ξ will probably depend on a number of factors, including the Mach number of the flow, the density structure of the secondary star and the effects of radiation pressure. Recent calculations by Kley, Shankar & Burkert (1995), which include the effects of radiation pressure and a realistic envelope structure for the secondary star, obtained drag coefficients (in our notation) of 0.3 and 5.8 respectively for wind temperatures of 2×10^6 and 2×10^5 K. The latter case is probably the more realistic; however, we assume $\xi=1$ as a conservative estimate.

The energy and angular momentum lost from the binary orbit are deposited into the wind in a toroidal region formed by the rotation of the accretion region about the centre of coordinates, and the subsequent flow is assumed to be axisymmetric. This is clearly an approximation to the real situation, although it is valid when the wind velocity is less than the orbital velocity; it is in this regime that the drag force has the greatest effect on the flow. The approximation is necessary in order to make the computations manageable.

3 NUMERICAL CALCULATIONS

The numerical code used to solve the hydrodynamic equations uses the second-order Godunov scheme due to Falle (1991). The equations are posed in $r-\theta$ spherical polar coordinates. The ϕ velocity is allowed to be non-zero, although axisymmetry is imposed so that all gradients in this direction are zero. Thus the code uses a '2.5D' approximation by allowing rotation about the symmetry axis, although constraining the flow to be axisymmetric. A small amount of numerical viscosity is required in order to control the effects of the Quirk instability (Quirk 1992) which afflicts codes based on the solution of Riemann problems when strong shocks propagate normally to a grid direction. This takes the form of a viscous component added to the fluxes derived from the Riemann problems, which depends on the difference of the hydrodynamic variables on either side of a cell boundary. This flux is therefore small in regions of smooth flow and affects only regions containing discontinuities.

The white dwarf is placed at the centre of coordinates, and the nova mass-loss is effected by means of a boundary condition at the inner radius of the grid. The orbit of the secondary about the white dwarf is assumed to be circular. The numerical grid consists of 400 radial cells and 100 cells in the θ direction. The radial grid spacing is uniform for the first 100 cells and increases by 2 per cent per cell thereafter. The smallest radial grid spacing (Δr_0) for each run is given in Table 1.

Energy and angular momentum are added in a region within one accretion radius of the secondary star, and the size of this region is updated at the beginning of each time-step. The fluid is assumed to be adiabatic.

Four runs of the code were performed, with the parameters listed in Table 1. The speed classes assigned to the models are based approximately on the relationship between speed class of a nova and the velocity of the principal shell (McLaughlin 1960). The white dwarf masses are also appropriate to the speed class, although this is important only for determining the orbital velocity. The values chosen for t_0 and t_1 are, in fact, not appropriate to even the fastest novae (being of order 1 d). However, computational constraints prevent the use of more appropriate values. In order to resolve adequately the flow within the binary system, the grid spacing is such that the maximum time-step dictated by the stability criterion for an explicit difference scheme is of order 1 s. The times chosen are sufficient for the flow in the region of the binary system to achieve an approximately steady state, and the shell morphologies produced by the model should therefore be reliable.

3.1 Model images

Images are produced from the hydrodynamic variables for times $t > t_1$ by integrating the square of the gas density along a grid of lines of sight. These synthetic images allow us to investigate the appearance of the remnant in the light of an optically thin transition in which the emission coefficient is proportional to the square of the density. Although we have only evolved the models for ~1 d, these images will give the morphology of the optical remnant in nebular lines at late times, as long as no further shaping occurs once the material is well outside the binary system.

4 NUMERICAL RESULTS

The results of the four runs are given in Figs 1–10. Figs 1–8 show the density field (remapped on to the meridional plane) at two evolutionary times for each of the four runs. In each case, results are shown for $t < t_0$ and for $t > t_1$. Figs 9 and 10 show grey-scale representations of the model images derived from the results at $t > t_1$ for each of the four runs.

Results from the first run, with parameters appropriate for a fast nova, are shown in Figs 1 and 2. Fig. 1 shows the region of the meridional plane surrounding the binary system (in this case the binary separation is 1.1×10^{11} cm) for $t < t_0$. A bow wave-like structure is formed around the secondary star, due to the expansion of hot material in the interaction region into the undisturbed wind. Material inside the bow wave is spun up and accelerated centrifugally, giving a higher wind velocity and hence a lower density at a given radius than in the undisturbed wind. This is the mechanism described by Lloyd, O'Brien & Kahn (1995) for

Table 1. Model parameters used for the numerical calculations.

	Run 1	Run 2	Run 3	Run 4
Speed Class	Fast	Mod. Fast	Mod. Fast	Slow
$v_0/\mathrm{km\ s^{-1}}$	1500	600	300	100
$v_1/\mathrm{km\ s^{-1}}$	4500	3000	2000	1000
$M_{WD}/M_\odot$	1.0	0.9	0.7	0.6
$M_2/M_\odot$	0.5	0.45	0.35	0.3
P_{orb}/hr	4.5	4.0	3.3	2.8
$\Delta r_0/10^9\mathrm{cm}$	3.0	3.0	2.0	2.0

All Runs - $\dot{M}_0/M_\odot\mathrm{yr}^{-1} = 2.5 \times 10^{-4}$
$\dot{M}_1/M_\odot\mathrm{yr}^{-1} = 3 \times 10^{-5}$
$t_0/s = 5 \times 10^4$
$t_1/s = 10^5$

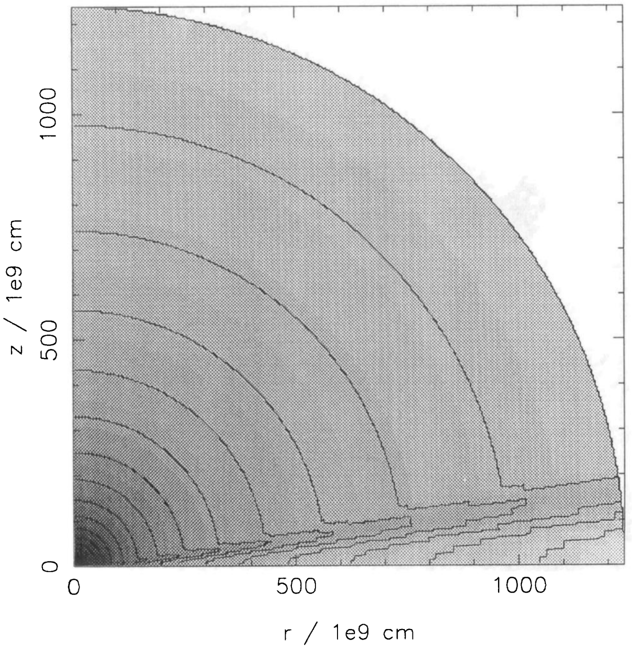

Figure 1. Grey-scale and contours of log density for Run 1 at a model time of 3.5×10^4 s.

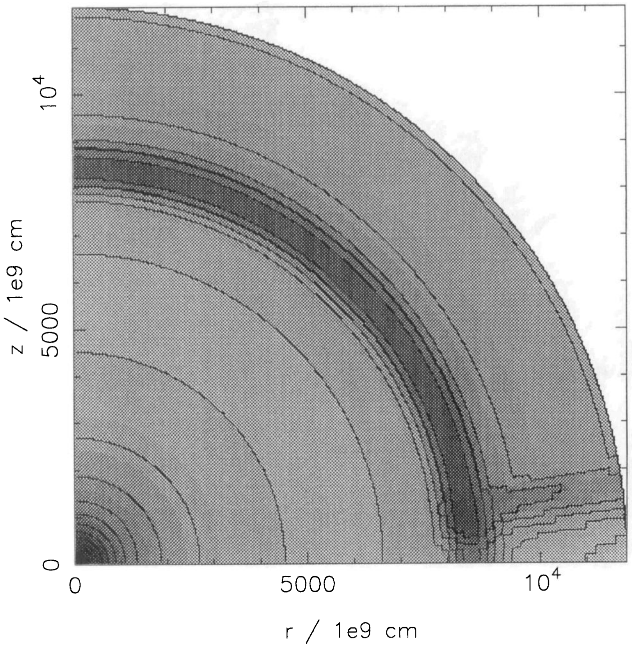

Figure 2. Grey-scale and contours of log density for Run 1 at a model time of 1.03×10^5 s.

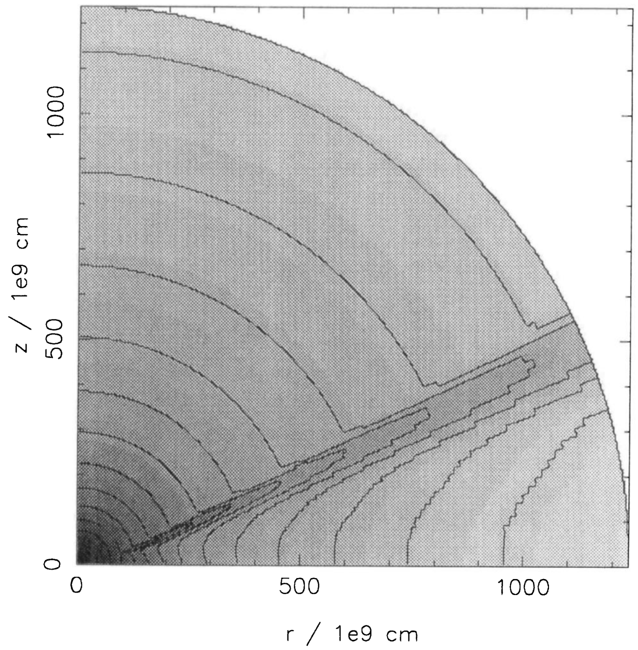

Figure 3. Grey-scale and contours of log density for Run 2 at a model time of 3.1×10^4 s.

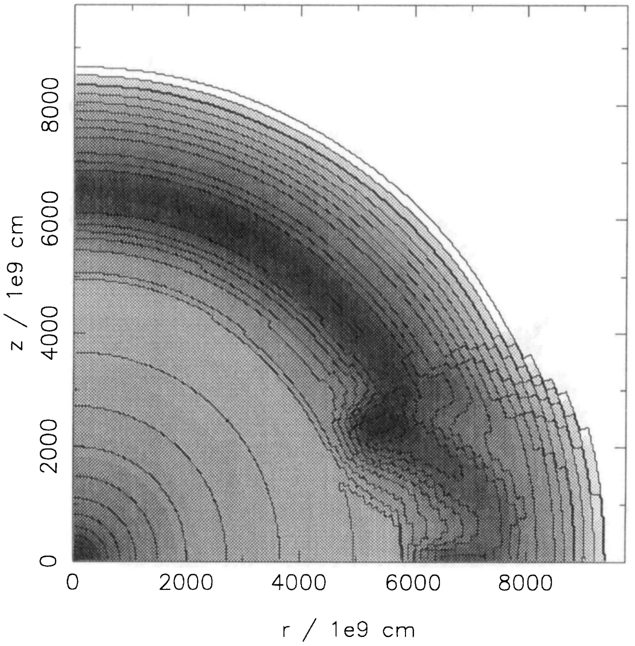

Figure 4. Grey-scale and contours of log density for Run 2 at a model time of 1.22×10^5 s.

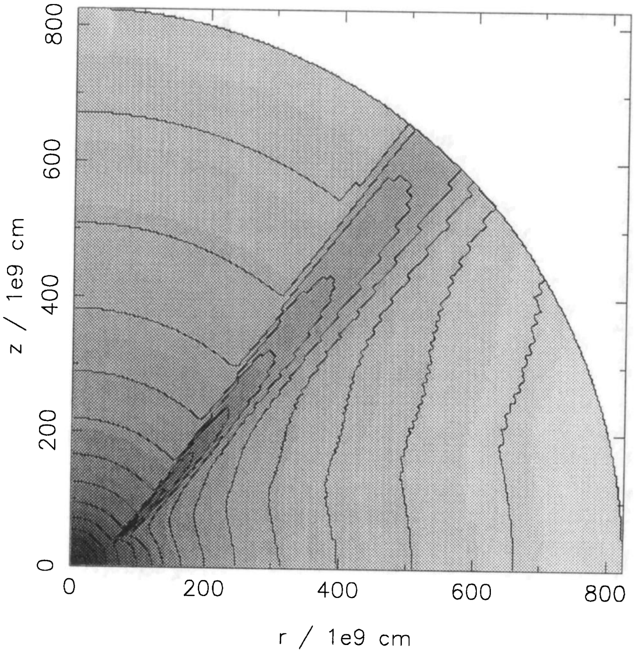

Figure 5. Grey-scale and contours of log density for Run 3 at a model time of 2.9×10^4 s.

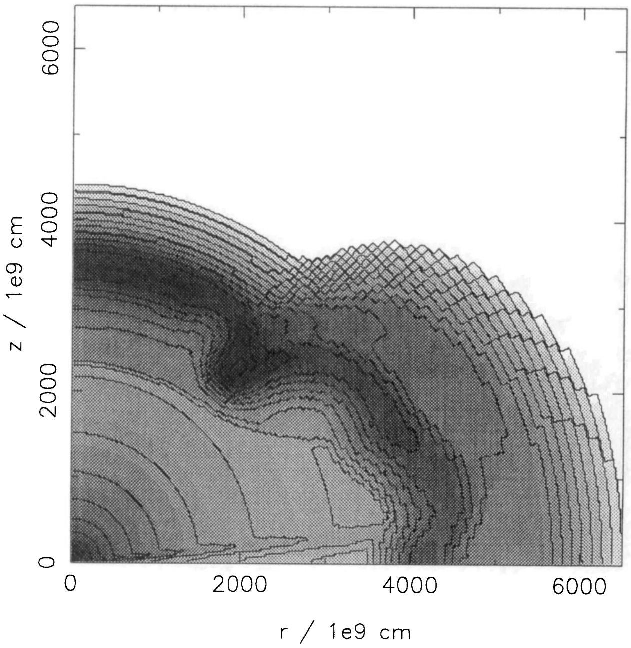

Figure 6. Grey-scale and contours of log density for Run 3 at a model time of 1.19×10^5 s.

producing a 'double-cone' structure in the wind of the progenitor of SN 1987a.

The situation after acceleration of the wind is shown in Fig. 2. The fast wind is largely unaffected by the drag force, and retains its spherical symmetry. The slow wind is swept up into a dense shell, which is also approximately spherically symmetric, although the density is enhanced where the shell sweeps up the bow wave structure in the slow wind. The synthetic image (Fig. 9) shows a roughly spherical nebula, with bands close to the equator corresponding to the density enhancements in the shell.

Figs 3 and 4 shows the results for Run 2. At early times a bow wave-like structure is formed around the secondary as in the previous run, although in this case the opening angle is larger due to the greater relative contribution of the drag luminosity compared with the mechanical luminosity of the wind. When this density distribution is swept up by the fast wind, an approximately spherical shell is produced, with

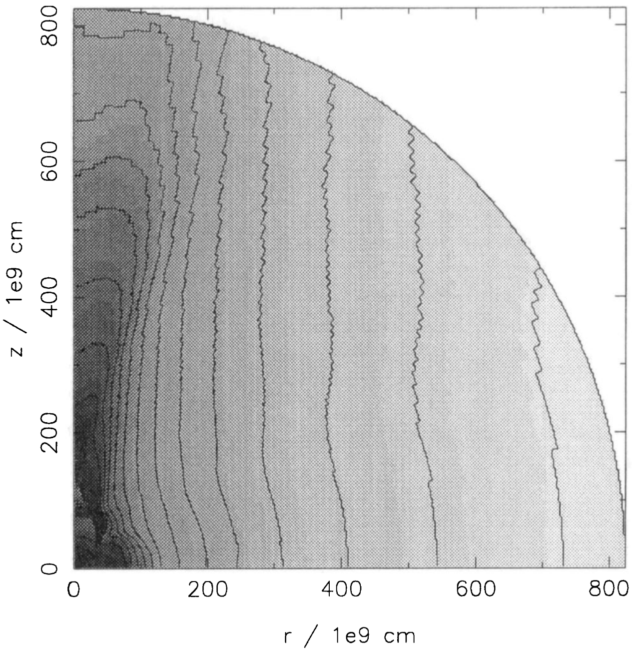

Figure 7. Grey-scale and contours of log density for Run 4 at a model time of 2.4×10^4 s.

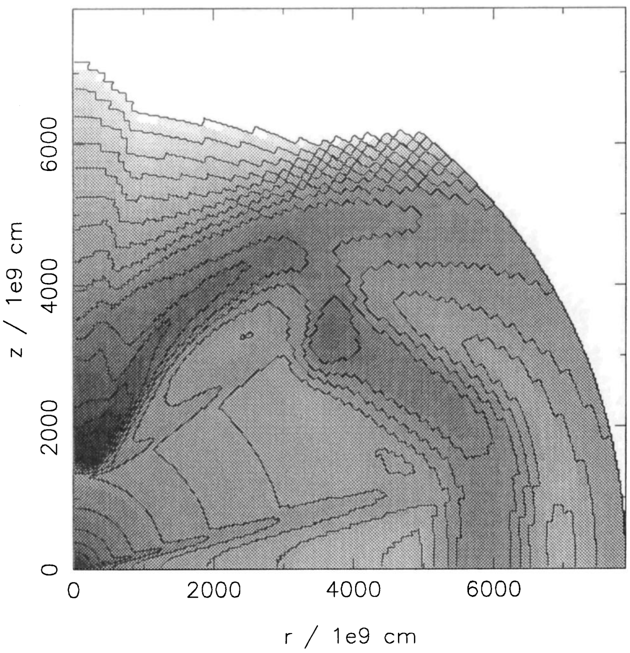

Figure 8. Grey-scale and contours of log density for Run 4 at a model time of 1.72×10^5 s.

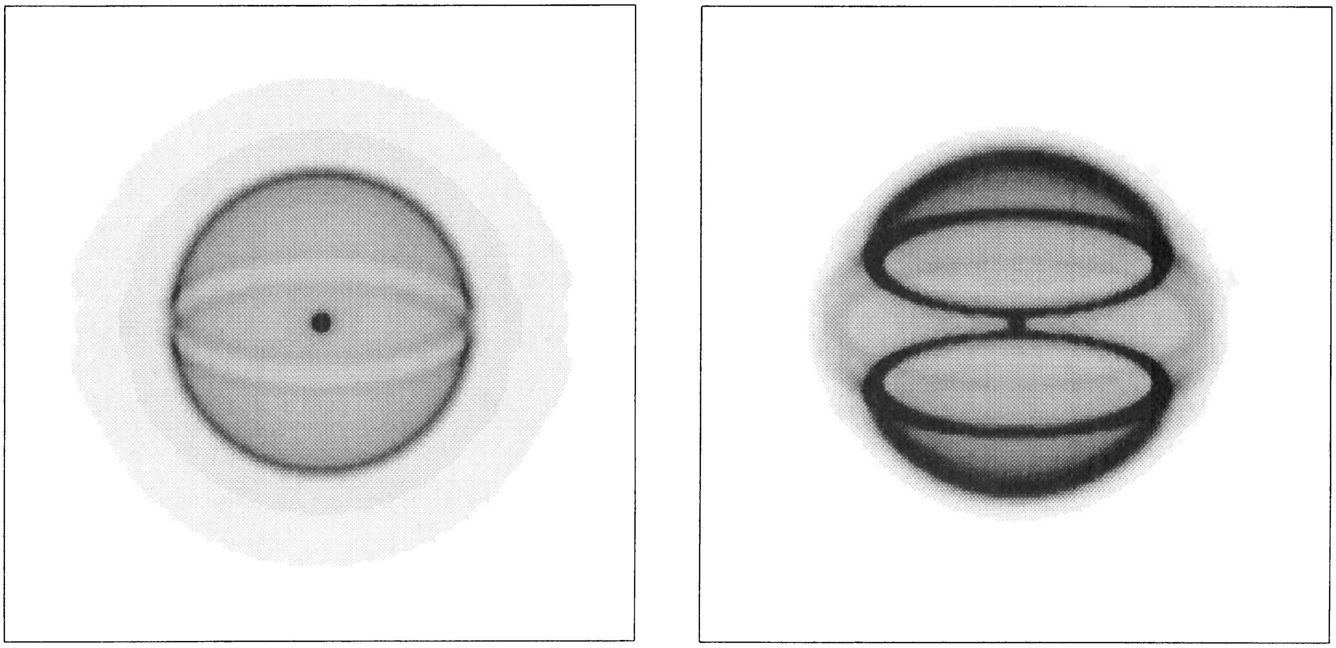

Figure 9. Synthetic images derived from the hydrodynamic solutions shown in Figs 2 and 4. The images are formed by integrating the square of the gas density along several lines of sight. The symmetry axis is inclined at an angle of 10° to the plane of the sky.

density enhancements at the points where the 'double cone' is being swept up. The synthetic image (Fig. 9) shows a shell with three pronounced rings – an equatorial ring and two tropical rings. The equatorial ring is due to centrifugally accelerated material ploughing into the back of the shell.

Similar structures are seen in Figs 5 and 6, which show the results for Run 3, although the opening angle of the bow wave around the interaction region is larger still. In this case, the image of the swept-up shell (Fig. 10) shows pronounced polar caps and rings. The emission from the rest of the shell is weak due to the low density in the evacuated region outside the 'double cone'.

Figs 7 and 8 show the results from Run 4. Here, the rate of drag heating is sufficiently large for the shock wave surrounding the interaction region to be forced on to the symmetry axis, where a dense pillar of shocked gas is formed. Although this feature has the appearance of a 'jet', the outflow velocity in this region is lower than its surroundings.

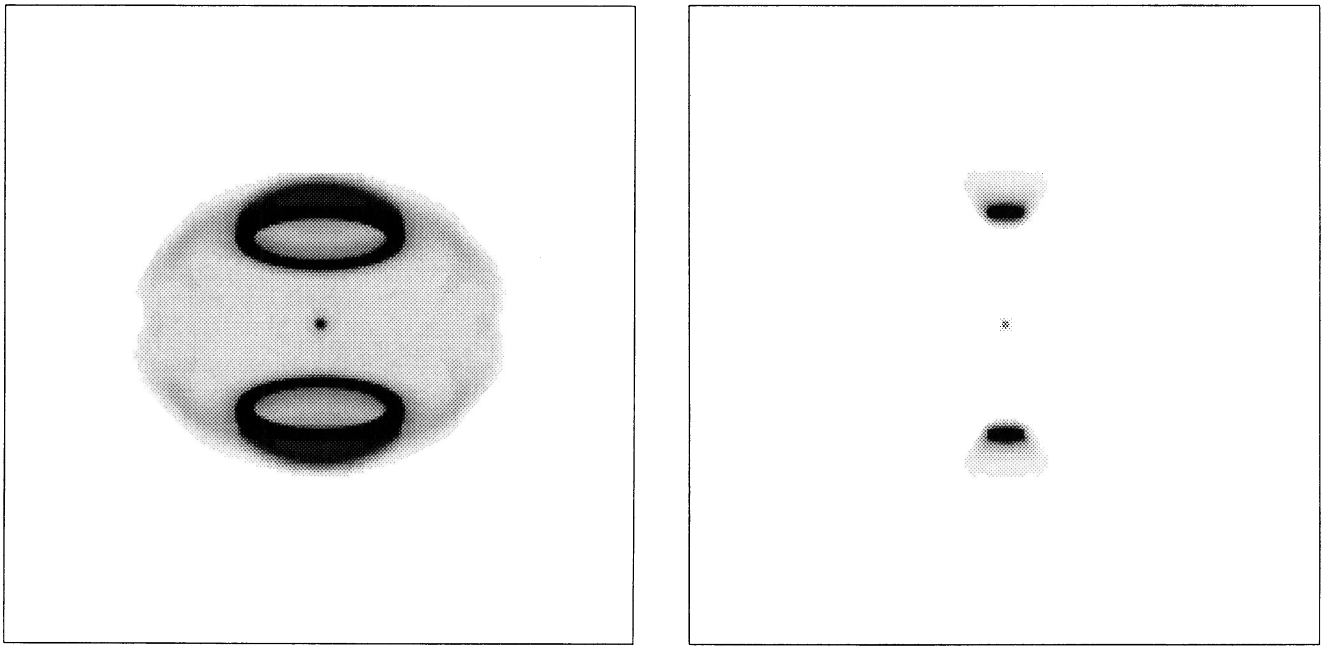

Figure 10. Synthetic images derived from the hydrodynamic solutions shown in Figs 6 and 8 (see Fig. 9 for details). The symmetry axis is inclined at an angle of 10° to the plane of the sky.

After acceleration of the wind, the fast wind sweeps up the slow wind into a shell which has a greatly enhanced density at the symmetry axis, where the dense polar pillar is being swept up. The synthetic image produced from these results (Fig. 10) is dominated by the enhanced density regions at the poles, which produce a pair of polar 'blobs'.

5 RADIATIVE COOLING

The hydrodynamical calculations described in this paper assume an adiabatic fluid; however, the shell of hot shocked gas produced in the interaction between the fast and slow winds is likely to radiate significantly in the soft X-ray, and these radiative losses could be dynamically important. In this section, we discuss the effects of radiative cooling, and the implications for the models.

We will assume that the shocked gas is in collisional ionization equilibrium, and we have calculated the cooling rate as a function of temperature using the code due to Raymond & Smith (1977). Two cases were calculated – enhanced carbon and oxygen, and enhanced oxygen, neon and magnesium. Nova ejecta are likely to be significantly enhanced in one of these two groups of elements, depending on whether the outburst takes place on a CO or an ONeMg white dwarf (see, e.g., Livio & Truran 1994). Elemental abundances for the ejecta of 18 novae are given by Livio & Truran (1994), with a mean heavy-element abundance (by mass) of $Z=0.31$, and a mean helium-to-hydrogen number ratio of 0.22. The abundances used to calculate our CO and ONeMg cooling curves assume a helium-to-hydrogen number ratio of 0.2, and enhanced CO or ONeMg (in solar ratios) such that $Z=0.33$.

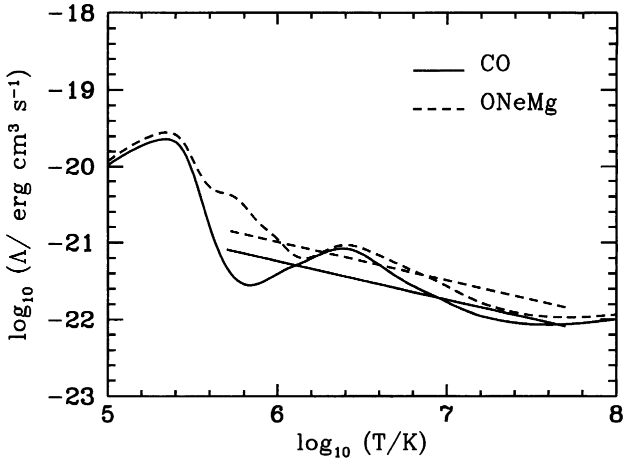

Figure 11. Plot of the cooling function Λ against temperature. The straight lines are the power-law fits to the cooling curves.

The volumetric cooling rate at a temperature T is given by

$$\dot{E}=\left(\frac{\rho}{m_{\mathrm{a}}}\right)^2\Lambda, \tag{5}$$

where ρ is the gas density and m_{a} is the mean mass of atoms and ions. The quantity Λ is plotted in Fig. 11, as a function of temperature. Between temperatures of 5×10^5 and 5×10^7 K, these cooling curves can be approximated well by the power law

$$\Lambda=\alpha T^{-1/2} \tag{6}$$

(Kahn 1976). Fitting power laws to the two cooling curves, we obtain

$$\alpha_{\mathrm{CO}}=5.75\times10^{-19}\ \mathrm{erg\ cm^3\ s^{-1}\ K^{1/2}} \tag{7}$$

and

$$\alpha_{\mathrm{ONeMg}} = 1.0 \times 10^{-18}\ \mathrm{erg\ cm^3\ s^{-1}\ K^{1/2}}. \tag{8}$$

The power-law fits are also plotted in Fig. 11. For both sets of abundances, the mean mass of particles $\bar{m} = 1.4 \times 10^{-24}$ g, and the mean mass of atoms and ions $m_{\mathrm{a}} = 3.6 \times 10^{-24}$ g.

In order to assess the effects of cooling in our interacting winds model, we will consider a shock with velocity v_{s} (in the frame of the central star) sweeping up a wind with velocity v_0, in the same frame. We will make the simplifying assumption that v_{s} is constant. The post-shock temperature T is related to v_{s} and v_0 by

$$v_{\mathrm{s}} - v_0 = \sqrt{\frac{16}{3}\frac{k_{\mathrm{B}}}{\bar{m}}T} \tag{9}$$

for a strong shock, where $\bar{m}$ is the mean mass of particles and k_{B} is Boltzmann's constant. The density behind the shock is four times the pre-shock density in the slow wind, and is therefore given by

$$\rho = \frac{\dot{M}_0}{\pi v_0 v_{\mathrm{s}}^2 t^2}, \tag{10}$$

where $\dot{M}_0$ and v_0 are the mass-loss rate and velocity of the slow wind, and t is the time since the onset of the fast wind. The cooling time is given by

$$t_{\mathrm{c}} = \frac{\rho k_{\mathrm{B}} T}{\bar{m}\dot{E}} = \frac{k_{\mathrm{B}} m_{\mathrm{a}}^2}{\bar{m}\alpha}\frac{T^{3/2}}{\rho}. \tag{11}$$

Substituting, we obtain

$$t_{\mathrm{c}} = \pi \left(\frac{3}{16}\right)^{3/2} \frac{m_{\mathrm{a}}^2 \bar{m}^{1/2}}{k_{\mathrm{B}}^{1/2}\alpha} \frac{v_0 v_{\mathrm{s}}^2 (v_{\mathrm{s}} - v_0)^3 t^2}{\dot{M}_0}. \tag{12}$$

The cooling time of newly-shocked gas is therefore initially short, and increases with time as the shock travels outwards in the slow wind. The shock will become adiabatic when $t_{\mathrm{c}} = t$, which happens at a time t_* after the onset of the fast wind, given by

$$t_* = \frac{1}{\pi}\left(\frac{16}{3}\right)^{3/2} \frac{k_{\mathrm{B}}^{1/2}\alpha}{m_{\mathrm{a}}^2 \bar{m}^{1/2}} \frac{\dot{M}_0}{v_0 v_{\mathrm{s}}^2 (v_{\mathrm{s}} - v_0)^3}. \tag{13}$$

From the numerical simulations, we find that typically $v_{\mathrm{s}} \sim 2v_0$ (i.e., the shell speed is approximately twice the slow wind speed). Taking $v_{\mathrm{s}} = 2v_0$, we obtain

$$t_* = \frac{1}{4\pi}\left(\frac{16}{3}\right)^{3/2} \frac{k_{\mathrm{B}}^{1/2}\alpha}{m_{\mathrm{a}}^2 \bar{m}^{1/2}} \frac{\dot{M}_0}{v_0^6}. \tag{14}$$

In order to investigate how the effects of cooling vary with speed class, we must first write $\dot{M}_0$ and v_0 as functions of t_3, the time to decline 3 mag from visual maximum. Following Livio (1992), we assume that the entire accreted envelope is ejected from the surface of the white dwarf, and that the mass of the envelope is given by (Truran & Livio 1986)

$$M_{\mathrm{e}} = \frac{4\pi P_{\mathrm{crit}}}{G}\frac{R_{\mathrm{wd}}^4}{M_{\mathrm{wd}}}, \tag{15}$$

where $P_{\mathrm{crit}} (= 2 \times 10^{19}\ \mathrm{dyn\ cm^{-2}})$ is the critical pressure required for a thermonuclear runaway, and M_{wd} and R_{wd} are the mass and radius of the white dwarf. The mass of the white dwarf in a nova system is related to t_3 by (Livio 1992)

$$t_3 = \tau \frac{M_{\mathrm{Ch}}}{M_{\mathrm{wd}}}\left[\left(\frac{M_{\mathrm{Ch}}}{M_{\mathrm{wd}}}\right)^{2/3} - \left(\frac{M_{\mathrm{wd}}}{M_{\mathrm{Ch}}}\right)^{2/3}\right]^{3/2}, \tag{16}$$

where M_{Ch} is the Chandrasekhar mass, and $\tau = 51.3$ d. The white dwarf radius R_{wd} is given by (Nauenberg 1972)

$$R_{\mathrm{wd}} = R\left[\left(\frac{M_{\mathrm{Ch}}}{M_{\mathrm{wd}}}\right)^{2/3} - \left(\frac{M_{\mathrm{wd}}}{M_{\mathrm{Ch}}}\right)^{2/3}\right]^{1/2}, \tag{17}$$

where $R = 1.2 \times 10^{-2} R_{\odot}$. Using equations (15), (16) and (17), we obtain

$$M_{\mathrm{e}} = \frac{4\pi P_{\mathrm{crit}}}{G}\frac{R^4}{M_{\mathrm{Ch}}}\left(\frac{t_3}{\tau}\right)^{4/3}\left[1 + \left(\frac{t_3}{\tau}\right)^{2/3}\right]^{-1/4}, \tag{18}$$

and to a reasonable approximation (given that t_3/τ is of order unity)

$$M_{\mathrm{e}} = \frac{4\pi P_{\mathrm{crit}}}{G}\frac{R^4}{M_{\mathrm{Ch}}}\left(\frac{t_3}{\tau}\right)^{4/3}. \tag{19}$$

Assuming that the bulk of the mass is lost in a time t_3, the mean mass-loss rate during this phase is given by

$$\dot{M}_0 = \frac{M_{\mathrm{e}}}{t_3}, \tag{20}$$

and hence

$$\dot{M}_0 = \frac{4\pi P_{\mathrm{crit}}}{G}\frac{R^4}{M_{\mathrm{Ch}}\tau^{3/4}} t_3^{1/3} = 7 \times 10^{20} t_3^{1/3}\ \mathrm{g\ s^{-1}}. \tag{21}$$

This mass-loss rate varies between several times $10^{-4}\ \mathrm{M_{\odot}\ yr^{-1}}$ for the fastest novae to $\sim 10^{-3}\ \mathrm{M_{\odot}\ yr^{-1}}$ for the slowest. Kovetz & Prialnik (1994) obtained an initial mass-loss rate of $2.5 \times 10^{-4}\ \mathrm{M_{\odot}\ yr^{-1}}$ from their thermonuclear runaway calculations for the case of a very fast nova, implying that the above analysis is reasonable.

We will take v_0 to be the velocity of the material responsible for the principal system of absorption lines. Empirically (McLaughlin 1960), this velocity is related to t_3 by

$$v_0 = 1.47 \times 10^{11} t_3^{-1/2}\ \mathrm{cm\ s^{-1}}, \tag{22}$$

where t_3 is in seconds. Substituting for $\dot{M}_0$, v_0, $\bar{m}$, m_{a} and k_{B}, we can now write t_*, from equation (14), in terms of t_3 as

$$t_* = 5.2 \times 10^4 \alpha t_3^{10/3}. \tag{23}$$

The other time-scale which must be considered is the time from the onset of the fast wind for the shock to reach the outer edge of the slow wind, at which time the shock 'blows out' into the low-density gas outside. This time, t_{b}, is equal to t_3 for $v_{\mathrm{s}} = 2v_0$. The quantity t_*/t_{b} is therefore given by

$$t_*/t_{\mathrm{b}} = 5.2 \times 10^4 \alpha t_3^{7/3}. \tag{24}$$

For CO novae, t_*/t_{b} is greater than unity for $t_3 > 7.2$ d, and for $t_3 > 5.7$ d in the case of ONeMg novae. Clearly, for all novae with $t_3 \gtrsim 5$ d, the shell will always be well cooled until the shock reaches the outer edge of the wind. Although we do not expect this to modify the shaping mechanisms described above, the effects of cooling will have implications for the final appearance of the shell. In particular, the flow behind the shock will possess oppositely directed pressure and density gradients if the cooling is strong, and will therefore be subject to the Rayleigh–Taylor instability. This will be the case if there is a non-positive radial density gradient behind the shock, because catastrophic cooling will always result in a positive radial pressure gradient. The cooling also serves to make the density gradient more negative.

The interaction region is not well resolved in these calculations, as the shock typically covers three grid cells whereas the interaction region covers about 15 cells. We have carried out a high-resolution simulation using the same code with 1100 radial grid cells in order to investigate the structure of the interaction region. The effects of the secondary star are neglected, and the fast wind is switched on instantaneously. In this calculation, we have taken $v_0 = 500$ km s^{-1}, $v_1 = 1500$ km s^{-1}, with the same values of $\dot{M}_0$ and $\dot{M}_1$ as before. Fig. 12 shows radial density and pressure profiles for the solution at a model time of 3×10^4 s after the onset of the fast wind. The reverse shock, contact discontinuity and forward shock are all well resolved. The pressure in the interaction region is approximately uniform, and there is a negative density gradient between the contact discontinuity and the forward shock. Hence, in the presence of strong cooling, we would expect this shell to become Rayleigh–Taylor unstable. Similar density and pressure profiles are found in the well-resolved 1D calculations of the interacting winds model described by O'Brien et al. (1994; see their fig. 1).

In this case, we would expect the shell to fragment, and the observed shell at late times will have a clumpy appearance. When the shell reaches the edge of the wind, the forward shock will accelerate outwards, whereas the cool shell will continue at constant radial velocity. Any remaining fast wind behind the shell will be able to stream unimpeded through the space between the clumps. This provides an appealing explanation for the appearance of the shells of DQ Her (Slavin et al. 1995) and RR Pic (O'Brien & Slavin 1995), which are highly clumped with 'cometary tails' extending radially outwards from the clumps into a diffuse halo. These tails could be formed by ablation of clump material as the fast wind streams through the shell. In the next section, we discuss the Rayleigh–Taylor instability in more detail.

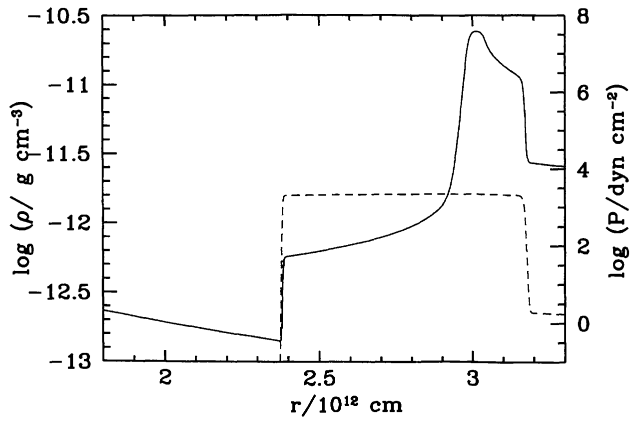

Figure 12. Radial profiles of density (solid line) and pressure (dashed line) for the high-resolution simulation (see Section 5 for details).

6 STABILITY OF THE SHELL

As discussed in the previous section, we would expect the shells formed in an interacting winds model of nova mass-loss would be well cooled, at least at early times in their evolution, and that this would give rise to oppositely directed density and pressure gradients behind the forward shock. This situation is unstable, and subject to the Rayleigh–Taylor instability. In this section, we will use some general arguments based on an incompressible Rayleigh–Taylor dispersion relation to investigate the stability of nova shells at early times in their evolution.

The Rayleigh–Taylor instability in incompressible fluids is discussed by Chandrasekhar (1961), who gives a dispersion relation for the growth of modes in a fluid which is exponentially stratified in the z direction, constrained between two plane-parallel surfaces and subject to an acceleration g. Although this is inappropriate to the case being considered here, we can at least use the results to gain some insight into the local stability at some point on a thin, spherically symmetric shell. The growth time, $\tau_{\rm RT}$, of the modes is given by

$$\tau^2_{\rm RT} = \frac{H}{g}\left[1 + \frac{1}{k^2H^2}\,(\delta + 1/4)\right], \qquad (25)$$

where H is the density scaleheight, g is the effective gravity, k is the wavenumber of the disturbance, and δ is given by

$$\delta = \left(\frac{m\pi H}{d}\right)^2. \qquad (26)$$

Here, m is a positive integer, and d is the physical size of the region. The effective gravity is given by

$$g = \frac{1}{\rho}\,\frac{\partial P}{\partial z}. \qquad (27)$$

We will assume that the density and pressure scaleheights are given by $r_{\rm c}$, the cooling length in the shell, and hence

$$g = \frac{1}{\rho}\,\frac{P}{r_{\rm c}}. \qquad (28)$$

Substituting for the post-shock pressure P, we obtain

$$g = \frac{3}{16}\,\frac{(v_{\rm s} - v_0)^2}{r_{\rm c}}. \qquad (29)$$

For $v_{\rm s} = 2v_0$,

$$g = \frac{3}{64}\,\frac{v_{\rm s}^2}{r_{\rm c}}. \qquad (30)$$

Writing $k=2\pi/\lambda$, we obtain

$$\tau_{\rm RT}^2=\frac{64r_{\rm c}^2}{3v_{\rm s}^2}\left[1+\frac{\lambda^2}{4\pi^2r_{\rm c}^2}(\delta+1/4)\right]. \tag{31}$$

Using $r=v_{\rm s}t$, and rearranging,

$$\left(\frac{\tau_{\rm RT}}{t}\right)^2=\frac{64}{3}\left(\frac{r_{\rm c}}{r}\right)^2\left[1+\frac{1}{4\pi^2}\left(\frac{\lambda}{r}\right)^2\left(\frac{r}{r_{\rm c}}\right)^2(\delta+1/4)\right]. \tag{32}$$

Thus the growth time increases with increasing wavelength, and the longest wavelength which is unstable is given by $\tau_{\rm RT}/t=1$. This wavelength, $\lambda_{\rm max}$, is given by

$$\left(\frac{\lambda_{\rm max}}{r}\right)=\frac{2\pi}{(\delta+1/4)^{1/2}}\left(\frac{r_{\rm c}}{r}\right)\left[\frac{3}{64}\left(\frac{r_{\rm c}}{r}\right)^{-2}-1\right]^{1/2}. \tag{33}$$

The shell will therefore be Rayleigh–Taylor unstable for $r_{\rm c}/r<\sqrt{3/64}$.

This analysis assumes an incompressible fluid. The incompressible result holds good for compressible fluids for wavenumbers $k>g/c_{\rm s}^2$, where $c_{\rm s}$ is the speed of sound in the gas, but the instability is severely damped for wavenumbers less than this value (Blake 1972). The maximum wavelength will therefore be given by the maximum of the expression given in equation (33), and a limiting value due to compressibility

$$\left(\frac{\lambda_{\rm max}}{r}\right)_{\rm c}=2\pi\gamma\left(\frac{r_{\rm c}}{r}\right), \tag{34}$$

where γ is the adiabatic index, and hence equation (33) is modified to

$$\left(\frac{\lambda_{\rm max}}{r}\right)=\min\left\{\frac{2\pi}{(\delta+1/4)^{1/2}}\left(\frac{r_{\rm c}}{r}\right)\left[\frac{3}{64}\left(\frac{r_{\rm c}}{r}\right)^{-2}-1\right]^{1/2},\ 2\pi\gamma\left(\frac{r_{\rm c}}{r}\right)\right\}. \tag{35}$$

We can now plot $\lambda_{\rm max}/r$ as a function of $r_{\rm c}/r$ (Fig. 13). To calculate δ, we have taken $m=1$ and d to be the thickness of the shell, given by the minimum of $r_{\rm c}$ and some fraction of r; we will take $d=\min(r_{\rm c},\ 0.2r)$. For $r_{\rm c}/r\lesssim 0.04$, the maximum unstable wavelength is limited by compressibility, and $\lambda_{\rm max}/r$ is proportional to $r_{\rm c}/r$ (from equation 34 above). For values of $r_{\rm c}/r$ greater than this, $\lambda_{\rm max}/r$ is given by equation (33), and decreases steadily from a maximum value of ~ 0.4. As $r_{\rm c}/r$ approaches $\sqrt{(3/64)}$, $\lambda_{\rm max}/r$ falls off rapidly to zero.

The cooling length $r_{\rm c}$ is given by the distance (in the frame of the post-shock gas), traversed by the shock in one cooling time. The shock velocity in this frame is $v_{\rm s}/4$, and hence $r_{\rm c}=t_{\rm c}v_{\rm s}/4$. The quantity $r_{\rm c}/r$ is therefore equal to $1/4(t_{\rm c}/t)$. From equation (12), substituting for $\dot{M}_0$ and v_0 from equations (21) and (22) with $\alpha=\alpha_{\rm ONeMg}$, we obtain

$$\frac{r_{\rm c}}{r}=\frac{1}{4}\,\frac{t_{\rm c}}{t}=4.7\times10^{12}t_3^{-10/3}t. \tag{36}$$

Thus $r_{\rm c}/r$ increases with time until the shock ‘blows out’ at a time $t_{\rm b}$ after the onset of the fast wind (for $v_{\rm s}=2v_0$, $t_{\rm b}=t_3$). The maximum unstable wavelength in the shell also increases linearly with time, until the shock reaches the edge of the slow wind (at $t_{\rm b}$) or $r_{\rm c}/r$ reaches a value of 0.04. A value of $r_{\rm c}/r=0.04$ is reached at $t_{\rm b}$ for a nova with $t_3=12.4$ d (from equation 36), and all novae slower than this (i.e., $t_3>12.4$ d) will always remain on the linear part of the $(\lambda_{\rm max}/r)$ versus $(r_{\rm c}/r)$ curve. The optical shell will be formed from the cooled gas behind the shock prior to blowout, and will be clumped on scales up to the value of $\lambda_{\rm max}/r$ at $t_{\rm b}$. For faster novae ($t_3<12.4$ d), the ratio of the longest wavelength of clumping to the radius of the shell will be fixed at the maximum value of $\lambda_{\rm max}/r$ (~ 0.4), assuming self-similar expansion. The longest clumping wavelength in the optical shell at late times (denoted L) can now be plotted as a function of t_3 (see Fig. 14), by calculating the value of $r_{\rm c}/r$ at blowout; if $r_{\rm c}/r$ at blowout is less than 0.04, then L/r is equal to $\lambda_{\rm max}/r$ from equation (24), otherwise L/r is equal to the maximum value of $\lambda_{\rm max}/r$ (see Fig. 13) of ~ 0.4.

Clearly, for the majority of novae, the maximum wavelength of the unstable modes is small compared to the radius of the shell and although the shell will be clumped,

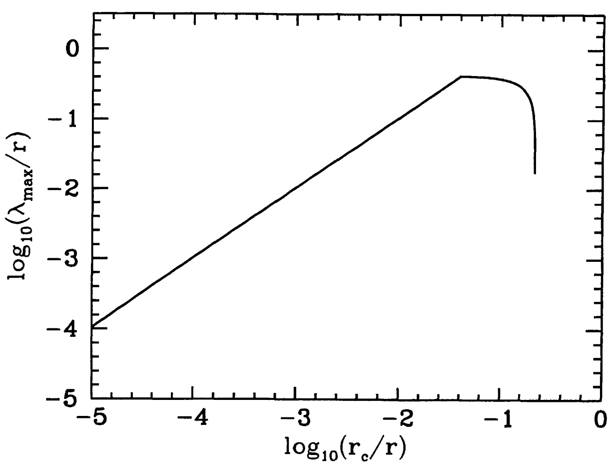

Figure 13. The variation of the maximum Rayleigh–Taylor unstable wavelength $\lambda_{\rm max}$ with cooling length $r_{\rm c}$; r is the shell radius.

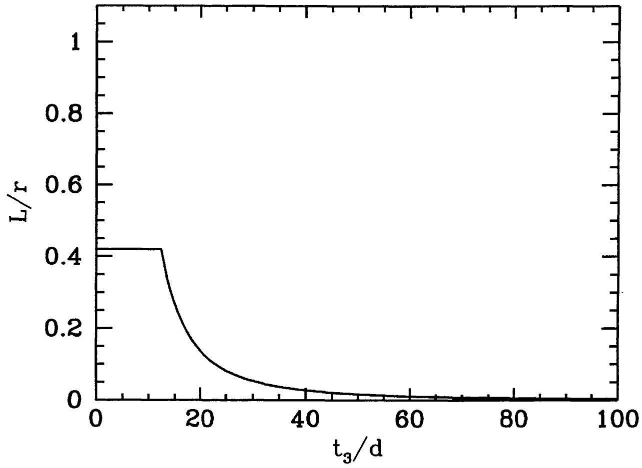

Figure 14. The maximum clumping wavelength L in terms of r, the shell radius, as a function of t_3, the time to decline 3 mag from maximum.

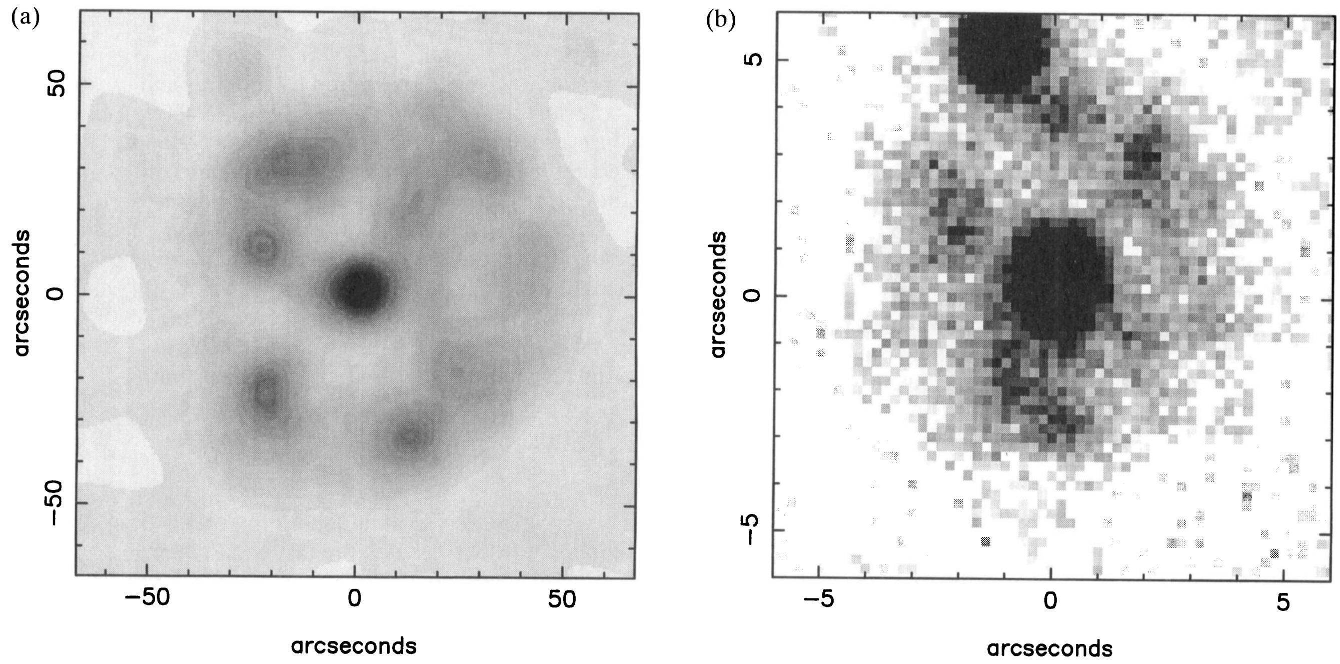

Figure 15. (a) N[II] image of the remnant of GK Per (from Slavin, O'Brien & Dunlop 1995, fig. 5c) smoothed to the same effective resolution as their Hα image of V1500 Cyg, reproduced here in (b).

the size of these clumps will be small (of the order of the shell thickness) and the overall morphology of the shell will be retained. For the fastest novae ($t_3 \lesssim 12$ d), however, we would expect the shell to be clumped on scales of order the shell radius, and the remnant will therefore break up into only a few discrete components. The predictions of this simple model are in general agreement with the observations. The deep optical images of nova shells made by Slavin et al. (1995) show that the remnants of very fast novae (e.g., V1500 Cyg, V476 Cyg) tend to comprise a few, randomly distributed clumps superposed on spherically symmetric diffuse material, whereas slower novae (e.g., FH Ser, DQ Her) show highly structured clumpy remnants with one or more bands of enhanced emission. It is interesting to note that the remnant of GK Per (a fast nova) is clumpy on very small scales. However, there is significant power on longer wavelengths – smoothing Slavin et al.'s (1995) N[II] image of this object to the same effective resolution as their image of V1500 Cyg results in a map which shows a few discrete emission components, bearing a remarkable resemblance to the shell of V1500 Cyg (see Fig. 15). If the clumps were distributed randomly, we would expect a uniform distribution in the smoothed map. Although the Rayleigh–Taylor instability may be responsible for forming the large-scale structure in the remnants of fast novae, the cooling gas will also be thermally unstable and condense further into smaller clumps which are resolved in the case of GK Per. The role of the thermal instability in clumping nova ejecta is discussed by Pistinner & Shaviv (1995).

7 DISCUSSION

In this paper, we have presented hydrodynamic calculations of the axisymmetric effects of the underlying binary system on a point-symmetric interacting winds model of classical nova mass-loss. The model treats the mass-loss as a wind with a velocity which increases in time, with an accompanying decrease in mass-loss rate. We find that the resulting shells can depart significantly from spherical symmetry, and that slower novae produce remnants which are more aspherical than those of faster novae, in agreement with observations.

The shaping effects are due to the transfer of angular momentum and energy from the binary orbit which result in the formation of a 'double-cone' structure in the wind from the white dwarf (see Lloyd et al. 1995). The opening angle of the cones varies with the wind speed, from almost π for $v_w \sim 1500$ km s^{-1} (giving a disc-like structure) to ~ 0 for $v_w \sim 100$ km s^{-1} (giving a polar 'pillar'). The time-variation of the wind speed gives rise to complex structures as fast material overruns slower material ejected earlier, which will have been subject to a greater degree of shaping.

The structures obtained in the model (with the relevant run numbers) include polar blobs (Run 4), polar rings (Run 3) banded shells (with equatorial and tropical rings, Run 2) and spherical shells (Run 1). All of these morphologies are seen in the shells of novae – candidate objects are HR Del (polar blobs), RR Pic (polar rings), DQ Her (equatorial and tropical rings) and GK Per (spherical shell). The speed classes of the models are all appropriate for the observational candidates. However, the shells obtained in this model are oblate, whereas the observed shells of novae are typically prolate. The effects of white dwarf rotation may explain the prolateness of nova shells (see, e.g., Ignace, Cassinelli & Bjorkman 1996 and Livio 1995). This would give rise to an equatorially enhanced slow wind, which would produce a prolate remnant when swept up by the fast wind. The shaping mechanisms described here will still operate to produce tropical and equatorial rings. Furthermore, the tropical rings produced in Run 2 are more pronounced than the equatorial ring, whereas the reverse is true in the observed shell of DQ Her; an equatorially enhanced slow wind may also remove this discrepancy. The effects of white dwarf rotation will be considered in a further paper. Another possibility is that further shaping takes place at times after the calculations presented here are terminated, although this may require the fast wind to be accelerated further, and a second episode of sweeping up to occur. This is another possible avenue for future investigation.

The role of radiative cooling has been considered. We have shown that the shells are Rayleigh–Taylor unstable, and we would expect them to fragment into a number of discrete clumps. When this happens, the fast wind will be able to stream unimpeded through the holes in the shell, which we suggest as an explanation for the extended haloes and 'cometary tails' seen in DQ Her (Slavin et al. 1995) and RR Pic (O'Brien & Slavin 1995). Furthermore, we find that the shells of moderately fast and slow novae should be clumped on length-scales comparable to the thickness of the shell, whereas the Rayleigh–Taylor instability in the fastest novae can form structures on length-scales comparable to the radius of the shell. In the latter case, we would expect the remnant to comprise a few, discrete emission regions, in agreement with the observations of V1500 Cyg and GK Per.

ACKNOWLEDGMENTS

HML is supported by a PPARC post-doctoral research assistantship. The numerical computations were carried out using the Liverpool JMU Starlink Node.

REFERENCES

Bath G. T., Harkness R. P., 1989, in Bode M. F., Evans A., eds, Classical Novae. Wiley & Sons Ltd., Chichester, p. 61
Blake G. M., 1972, MNRAS, 156, 67
Bode M. F., Evans A. E., 1989, Classical Novae. Wiley & Sons Ltd, Chichester
Chandrasekhar S., 1961, Hydrodynamic and Hydromagnetic Stability. Oxford Univ. Press, London
Falle S. A. E. G., 1991, MNRAS, 250, 581
Ignace R., Cassinelli J. P., Bjorkman J. E., 1996, ApJ, 459, 671
Kahn F. D., 1976, A&A, 50, 145
Kato M., Hachisu I., 1994, ApJ, 437, 802
Kley W., Shankar A., Burkert A., 1995, A&A, 297, 739
Kovetz A., Prialnik D., 1994, ApJ, 424, 319
Livio M., 1992, ApJ, 393, 516
Livio M., 1995, in Buckley D. A. H., Warner B., eds, Cape Workshop on Magnetic Cataclysmic Variables, ASP Conference Series No. 85. Astron. Soc. Pac., San Francisco
Livio M., Soker N., 1988, ApJ, 329, 764
Livio M., Truran J. W., 1994, ApJ, 425, 797
Livio M., Shankar A., Burkert A., Truran J. W., 1990, ApJ, 356, 250
Lloyd H. M., O'Brien T. J., Bode M. F., Predehl P., Schmitt J. H. M. M., Trümper J., Watson M. G., Pounds K. A., 1992, Nat, 356, 222
Lloyd H. M., O'Brien T. J., Kahn F. D., 1995, MNRAS, 273, L19
MacDonald J., 1980, MNRAS, 191, 933
MacDonald J., 1986, ApJ, 305, 251
McLaughlin D. B., 1960, in Greenstein J. L., ed., Stellar Atmospheres. Univ. Chicago Press, Chicago, p. 585
Nauenberg M., 1972, ApJ, 175, 417
O'Brien T. J., Slavin A. J., 1996, in Wood J. H., Evans E., eds, Cataclysmic Variables and Related Objects. Kluwer, Dordrecht, p. 309
O'Brien T. J., Lloyd H. M., Bode M. F., 1994, MNRAS, 271, 155
Pistinner S., Shaviv G., 1995, ApJ, 448, L39
Prialnik D., Kovetz A., 1995, ApJ, 445, 789
Quirk J. J., 1992, A Contribution to the Great Riemann Solver Debate. ICASE Technical Report 92-64, NASA, Langley
Raymond J. C., Smith B. W., 1977, ApJS, 35, 419
Shankar A., Livio M., Truran J., 1991, ApJ, 374, 623
Slavin A. J., O'Brien T. J., Dunlop J. S., 1995, MNRAS, 276, 353
Truran J., Livio M., 1986, ApJ, 308, 721